











RESEARCH ARTICLE

Novel 8%-TiO₂-nanoparticle-reinforced dense polycrystalline bovine hydroxyapatite bioceramic

Lucas José de Azevedo-Silva¹  | Brunna Mota Ferrairo¹  | Luara Aline Pires²  |
David Santos Souza Padovini³  | Leonardo Francisco Gonçalves Dias⁴  |
Rogério Erbereli⁵  | Carlos Alberto Fortulan⁵  | Paulo Noronha Lisboa-Filho⁴  |
José Henrique Rubo¹  | Ana Flávia Sanches Borges² 

¹Department of Prosthodontics, Bauru School of Dentistry, University of São Paulo, Bauru, Brazil

²Department of Operative Dentistry, Endodontics and Dental Materials, Bauru School of Dentistry, University of São Paulo, Bauru, Brazil

³Department of Chemistry, School of Sciences, São Paulo State University, Bauru, Brazil

⁴Department of Physics, School of Sciences, São Paulo State University, Bauru, Brazil

⁵Department of Mechanical Engineering, São Carlos School of Engineering, University of São Paulo, São Carlos, Brazil

Correspondence

Ana Flávia Sanches Borges, Department of Operative Dentistry, Endodontics and Dental Materials, Bauru School of Dentistry, University of São Paulo, Alameda Dr. Octávio Pinheiro Brisolla, 9-75, Vila Universitária, Bauru, São Paulo 17012-901, Brazil.
Email: afborges@fob.usp.br

Funding information

Conselho Nacional de Desenvolvimento Científico e Tecnológico, Grant/Award Number: 154705/2015-2; Fundação de Amparo à Pesquisa do Estado de São Paulo, Grant/Award Numbers: 2013/07296-2, 2018/23639-0, 2020/01715-7

Abstract

This study aimed to produce and characterize the microstructure and mechanical properties of dense polycrystalline bovine hydroxyapatite (DPBHA) bioceramics with 5% and 8% of TiO₂ nanoparticles after final sinterization for future use in dental implants. Structural characterization was obtained from analyzes by Fourier transform infrared spectroscopy, X-ray diffraction, scanning electron microscope, energy dispersive spectroscopy, and relative density and apparent porosity. The mechanical characterization was performed by measuring the fracture toughness after three-point flexural strength (FS) test. The microstructural characterization results showed no secondary phase formation and nonhomogeneous nanoparticle dispersion in HA matrix. DPBHA/Np8% ($2.9 \pm 0.09 \text{ g/cm}^3$) exhibited significantly greater density than DPBHA ($2.7 \pm 0.03 \text{ g/cm}^3$) ($p = 0.011$) and DPBHA/Np5% ($2.7 \pm 0.05 \text{ g/cm}^3$) ($p = 0.041$). DPBHA (0.9%) had the smallest porosity followed by DPBHA/Np8% (3.4%). DPBHA/Np5% (4.5%) exhibited the greatest proportion of pores. Pure HA ($51.7 \pm 10.3 \text{ MPa}$) and DPBHA/Np8% ($47.4 \pm 6.4 \text{ MPa}$) had significant greater FS ($p < 0.001$) than DPBHA/Np5% ($28.8 \pm 3.1 \text{ MPa}$). DPBHA ($0.43 \pm 0.01 \text{ MPa m}^{1/2}$) and DPBHA/Np8% ($0.40 \pm 0.06 \text{ MPa m}^{1/2}$) presented greater K_{IC} than DPBHA/Np5% ($0.23 \pm 0.02 \text{ MPa m}^{1/2}$) ($p < 0.003$; $p < 0.007$). In conclusion, 8% TiO₂ nanoparticle addition to this synthesis would be a promising HA blend, as mechanical properties were similar, and the relative density/apparent porosity showed superior results than those of the DPBHA.

KEYWORDS

bioceramics, hydroxyapatite, nanoparticles

This is an open access article under the terms of the [Creative Commons Attribution](https://creativecommons.org/licenses/by/4.0/) License, which permits use, distribution and reproduction in any medium, provided the original work is properly cited.

© 2022 The Authors. *International Journal of Ceramic Engineering & Science* published by Wiley Periodicals LLC. on behalf of the American Ceramic Society.

1 | INTRODUCTION

Aiming to achieve a balance between sustainable development and wellness, researchers worldwide are asking the question: how can we contribute to developing products from renewable sources? Bovine bones, for instance, can be a renewable source of hydroxyapatite (HA), since they would be discarded and could be used as a raw material for HA extraction.^{1–4}

In an attempt to produce a novel dense polycrystalline bovine HA bioceramic (DPBHA) for possible use as dental implants or dental prosthesis, this experimental material showed suitable osteoblast cell adhesion, as well as cell viability.⁵ Regarding mechanical properties, DPBHA reached biaxial flexural strength (FS) about 235.2 MPa, Vickers hardness about 335 GPa, and a high Weibull modulus (m), and characteristic life (σ_0).⁶ Yttria-stabilized tetragonal zirconia polycrystal (Y-TZP) microstructure is similar to that of DPBHA but with higher mechanical values, ranging from 680 to 1200 MPa of FS^{7–13} and from 3.17 to 8 MPa.m^{1/2} of fracture toughness.¹⁴

Seeking for improving one of the most important mechanical properties from ceramic materials, fracture toughness, which measures the stress concentration at a crack tip (intensity factor - K_{IC} ¹⁵), TiO₂, ZnO, Y-TZP, Al₂O₃, and graphene at nanoscale have been added to reinforce ceramic materials.^{6,7,16–18} For DPBHA, the mechanisms of nanostructure reinforcement are crack deflection, leading to energy absorption from the crack and tensile stress at the crack's tip.^{18–20} Zirconia, alumina, mullite, titanium, and bioglass have been added to HA.^{18–28} Pires et al.⁶ added ZnO and TiO₂ nanoparticles and TiO₂ nanotubes into bovine HA, showing that TiO₂ nanoparticles yielded higher biaxial FS results through its microstructural organization. TiO₂ nanoparticles have been considered as a reinforcement for ceramics^{29–32} because of their advantages, such as chemical stability,^{29,30} photocatalysis, antimicrobial performance,^{29–31} and biocompatibility.³² In addition, TiO₂ nanoparticles improved grains' growth, Vickers hardness, and densification when added to ZrO₂ bioceramics.^{33,34} The material microstructure guides the ceramic materials' mechanical properties.

Therefore, this study aimed to evaluate TiO₂ nanoparticles effects to the novel DPBHA microstructure and physicochemical properties. The study hypothesis was that this addition would modify (1) the microstructure, (2) relative porosity, (3) FS, and fracture toughness of the novel DPBHA.

2 | EXPERIMENTAL PROCEDURES

2.1 | Preparation of specimens

2.1.1 | Preparation of TiO₂ nanoparticles

TiO₂ nanoparticles were obtained by a chemical process (adapted from Arruda et al.³⁵). Distilled water (185 ml), isopropanol (LabSynth; 56.7 ml), and nitric acid (HNO₃, Sigma Aldrich; 2.6 ml) were added into an Erlenmeyer flask. Next, 15 ml of titanium (IV) isopropoxide (Sigma Aldrich) was added to the above solution, and the contents were stirred at 300 rpm for 30 min. In addition, the solution was heated to 85°C, while stirring. The heating and stirring were continued until a complete evaporation of the liquid, and the resultant crystallization took place. Subsequently, the crystals were placed in a furnace and reduced to a homogeneous powder.

2.1.2 | HA powder preparation

The materials used in the manufacturing of the developmental ceramic material were polyvinyl butyral (PVB; Butvar B98) as a binder, 4-aminobenzoic acid (PABA; Sigma Aldrich) as a deflocculant, and isopropyl alcohol (LabSynth) as a solvent of the binder, as well as a liquid barbotine medium (Table 1).

Metatarsus specimens from a 2-year-old bovine were collected and passed through an initial manual cleaning. Subsequently, they were subjected to a thermochemical process, with hydrogen peroxide (H₂O₂) as a 30 %, 100 volume aqueous solution, and heated to 100°C. Then, the bones were calcined with a heating curve up to (5°C/min)

TABLE 1 Density and proportion of components used in specimens' preparation

Component	Density (g/cm ³)	Proportion (%)	Function
HA	3.14	30% (total volume)	Ceramic powder
PABA (4-Aminobenzoic acid)	1.37	0.05% (ZrO ₂ weight)	Deflocculant
Polyvinyl butyral (PVB)	1.1	2% (ZrO ₂ weight)	Binder
Isopropyl alcohol	0.78	70% (total volume)	Solvent
TiO ₂ nanoparticles	4.23	5 and 8% (total volume)	Reinforcement

Abbreviations: HA, hydroxyapatite; PABA, para-aminobenzoic acid.

900°C, to residual organic matter removal. This resulted in the production of a particulate HA. Next, in an alcohol environment, two types of milling were performed on the HA. In the first milling, a jar was loaded with 30 vol% of HA, 69.95 vol% of isopropyl alcohol, and 0.05 wt% of para-aminobenzoic acid (PABA). This mixture was placed in a rotatory mill for 48 h, after which it was vibrated in a ball mill for 96 h.

Next, 1.2 wt% of PVB, dissolved in isopropanol, was added and homogenized in a vibratory mill for 2 h. For the specimens added with nanomaterials, after these 2 h in the vibrating mill, the nanoparticles were weighed at 5% and 8% of the working volume relative to HA, and added to smaller HA-loaded jars. The mixtures were returned to the vibrating mill for 10 min.

After the second milling, each jar was discharged, and the barbotine was dried with a hot air blower at approximately 80°C. The mixtures were granulated in a sieve (# 200 with a mesh size $\leq 75 \mu\text{m}$) to obtain granules with an average size of $35 \mu\text{m}$.

2.1.3 | Ceramic bar preparation

The experimental groups used were DPBHA, DPBHA/Np5%, and DPBHA/Np8% (the last two containing, respectively, 5% and 8% of TiO_2 nanoparticles). The chosen amounts were based on previous promising use of TiO_2 nanoparticle results for HA.⁶ For the preparation of the sample, 1.5 g of these powders was weighed, placed in a rectangular device, and subjected to compaction by uniaxial pressing at 100 MPa for 1 min to generate specimens with 21-mm length, 4-mm width, and 3-mm height.

The specimens were then encapsulated under vacuum in an elastomeric film and pressed by an isostatic press at 200 MPa for 1 min. Next, the specimens were subjected to a sintering process in a Lindberg Blue/M chamber-type furnace in an air atmosphere. The successive step-wise increase in the temperature was as follows: first, from ambient temperature to 160°C at a heating rate of 2.7°C/min; from 160 to 600°C at 4°C/min; from 600 to 1100°C at 5°C/min; and finally, from 1100 to 1300°C at 6°C/min. The specimens were maintained at the maximum temperature of 1300°C for 120 min, after which, they were slowly cooled to the ambient temperature.

2.2 | Structural analyses

2.2.1 | X-ray diffraction

For the detection of the crystalline phase using X-ray diffraction (XRD), the original powders and the sintered

specimens were positioned in a specimen holder to ensure smooth surfaces and mounted on a fixed horizontal specimen plane. The spectra were recorded at the ambient temperature on a Philips X' Pert X-ray diffractometer with a $\text{Cu K}\alpha$ source ($\lambda = 1.5418 \text{ \AA}$) in Bragg–Brentano geometry (2θ). The data analyses were carried out using the profile fits of selected individual XRD peaks.

2.2.2 | Fourier transform infrared spectroscopy

The ceramic powder sintered specimens were subjected to spectroscopy on infrared frequency (Vertex 70, Bruker). Using this technique, the vibration bands that occurred between 4000 and 400 cm^{-1} were observed.

2.2.3 | Field emission scanning electron microscope/energy dispersive spectroscopy

Five specimens from each group were randomly selected after testing and then gold-sprayed for a scanning electron microscope (SEM) analysis (ZEISS, Supra40, Jena, Germany). The measurements were taken on the fractured surfaces at $\times 80$, $\times 200$, $\times 400$, and $\times 3000$ magnifications. The composition measurements by energy dispersive spectroscopy (EDS) were taken at $\times 3000$ magnification at the external and fractured surfaces in the bar specimens and in the original powders.

2.2.4 | Relative density and apparent porosity ($n = 10$)

The relative density and apparent porosity were measured using the Archimedes principle. This methodology required mass measurements under three different conditions for each specimen, namely dry, wet, and liquid-immersed.

The density values were obtained with the following equation for each specimen:

$$\rho_{\text{specim}} = \frac{w_d}{(w_w - w_l)} \times \rho_{\text{liquid}} \quad (1)$$

where ρ is the specimen density, w_d is the dry specimen weight, w_w is the wet specimen weight, w_l is the liquid immersion specimen weight, and ρ is the density of the liquid used for the specimen immersion.

The porosity values were obtained with the following equation for each specimen:

$$Ap(\%) = \frac{w_w - w_d}{(w_w - w_l)} \times 100 \quad (2)$$

where A_p is the specimen porosity, w_w is the wet specimen weight, w_d the dry specimen weight, and w_l is the liquid immersion specimen weight.

2.3 | Mechanical analyses

2.3.1 | Flexural Strength (FS) ($n = 10$)

The specimens were beveled using a metal device, whereby the four largest edges of each specimen were beveled to a standard width of 0.1 mm in accordance with ISO 6872 (2015).³⁶

A three-point FS test (σ_f) of the bar specimens was performed on a universal testing machine (Sintec 5G, MTS systems corporation) with a 5000 N compression load and a constant speed of 0.5 mm/min. The specimens were positioned in a three-point flexure device with a distance of 12.0 mm between each of the support cylinders and the center of the metal sphere, where the load was applied. The FS(σ_f) was determined according to the equation: $\sigma_f = 3Pl/2wb^2$, where P is the fracture load (N), l is the distance between the supports, that is, span and is equal to 12 mm, w is the specimen width (mm), and b is the specimen thickness (mm).

2.3.2 | Fracture toughness by flexural surface fracture (FT) ($n = 10$)

The fractured specimen surfaces were first cleaned using ultrasound by immersing the specimens in a detergent solution for 15 min (adapted from Cesar et al.,¹⁵ and Ramos et al.³⁷). This is followed by an immersion for 15 min in a bath with deionized water and 100% ethanol. The specimen surfaces were examined under a stereomicroscope (Leica 0.45X, Meiji Techno, Japan) to determine the location of the origin of the fracture.

The size of the critical defect (c) was measured (Image J, Wayne Rasband, USA) at $\times 200$ magnification, and a quantitative analysis was conducted based on the following equation:

$$c = (ab)^{1/2}, \quad (3)$$

where a is the height of the origin of the defect and b is the half width.³⁸

The fracture toughness KIc was estimated using the FS σ_f by applying the fracture mechanics principles.

Equation 3 was used for the calculation, based on the Griffith–Irwin theory^{39,40}:

$$KIc = Y\sigma_f\sqrt{a}. \quad (4)$$

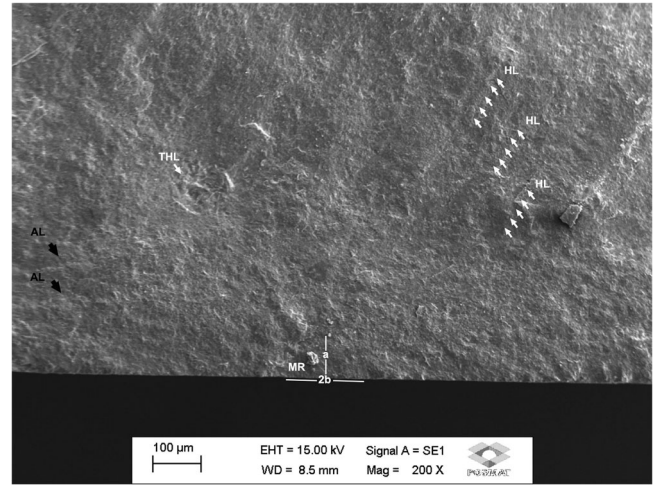


FIGURE 1 Fractured surface of DPBHA. Schematic critical defect was measured by defining characteristic areas for fractographic analysis. Hackle lines (HL), Twisted Hackle Lines (THL), Arrest Lines (AL) and Mirror Region (MR) were indicated by arrows

Where KIc is the fracture toughness ($\text{MPa}\cdot\text{m}^{1/2}$), σ_f is the resistance to fracture (MPa), Y is the geometric factor of stress intensity (related to the defect geometry), c is the defect size; and Y is a parameter that considers the location and shape of the initial defect and is calculated according to American Society for Testing and Materials (ASTM) C1421 standard. (Figure 1).

2.4 | Statistical analyses

Data were submitted to the Kolmogorov–Smirnov and Shapiro–Wilk normality tests. The Levene test was performed to verify the homogeneity of the variances. After the verification of normality, data were analyzed by ANOVA at $\alpha = 0.05$, followed by the Tukey test for comparison among groups.

3 | RESULTS

3.1 | XRD

XRD results are shown in Figure 2. XRD spectrum identified predominance in the crystallographic plane characteristics of HA (card number: 00-009-0432). The presence of TiO_2 phase peaks was also observed (card number: 00-002-0494) in a secondary and tenuous, but defined state, as it was present in only a small amount in HA matrix. The coexistence of HA and TiO_2 could also be observed in the specimens with the nanoparticle addition. Therefore, there was no transformation into a secondary phase.

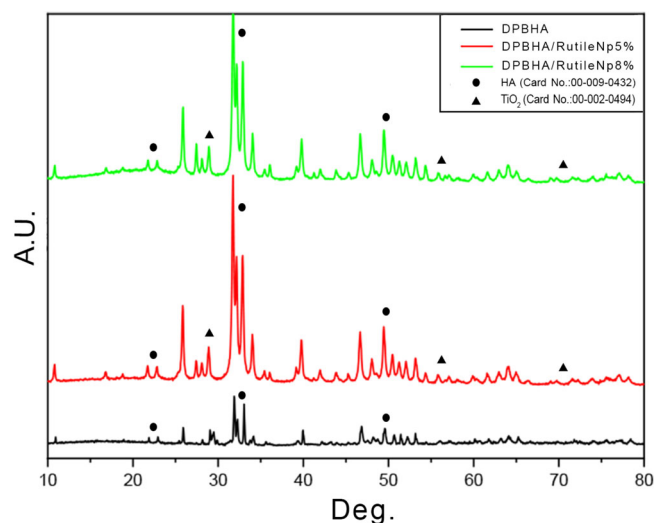


FIGURE 2 X-ray diffraction (XRD) patterns of pure dense polycrystalline bovine hydroxyapatite (DPBHA), DPBHA/Np5%, and DPBHA/Np8%. (card numbers: 00-009-0432 and 00-002-0494)

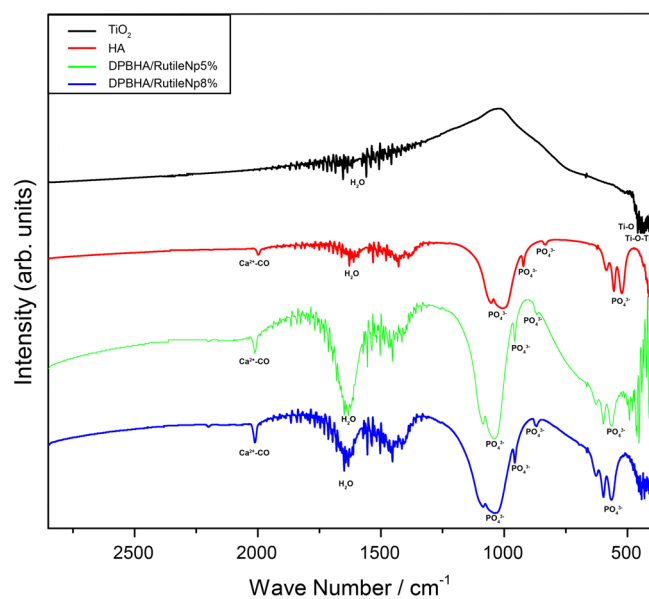


FIGURE 3 Fourier transform infrared (FTIR) spectra of starting ceramic powder before sintering process

3.2 | Fourier transform infrared spectroscopy

The Fourier transform infrared spectroscopy (FTIR) results show the chemical bonds in the materials by means of the bonds (Figures 3 and 4). Initially, after the calcination and sintering steps, the residual organic matter and the used solvents/reagents were eliminated.

In all the specimens, bands attributed to PO_4^{3-} groups (1101 , 1026 , 633 , and 560 cm^{-1}) could be noticed; the band at 1650 cm^{-1} was attributed to the H_2O bonds; the band at

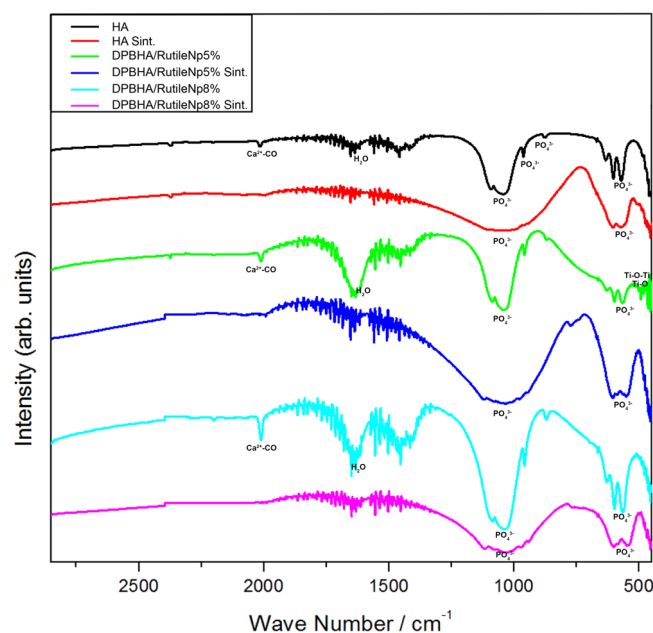


FIGURE 4 FTIR spectra of starting ceramic powder before sintering process

2300 cm^{-1} was attributed to the atmospheric CO_2 ; and the band at 1545 cm^{-1} was attributed to the CO_3^{2-} ions. This could be caused by the dissolution of atmospheric CO_2 during the synthesis.⁴¹ The band at 2010 cm^{-1} was attributed to the Ca^{2+} -CO bond.⁴²

The TiO_2 nanoparticles could be noticed from the Ti-O-Ti and Ti-O bonds from 450 to 500 cm^{-1} .⁴³ As seen in the XRD results, there was no link between Ti and any chemical element present in HA.

In the start ceramic powder spectra, a stretched 1650 cm^{-1} band could be noticed in nonsintered specimens, due to the absorbed water. This pattern was not observed in the sintered specimens. The Ti-O-Ti and Ti-O bonds were only observed in the sintered specimen with 5% TiO_2 . In the other specimens, these bands may deviate to a frequency below 500 cm^{-1} . According to the literature, such connections could be observed from 400 to 700 cm^{-1} .⁴³ This fact may also be due to the low amount of titanium in the samples and the low detection limit of the methodology.

3.2.1 | Field emission SEM/EDS

The field emission-SEM images ($\times 3000$ magnification) of the fractured surface show a similarity between the pure DPBHA and DPBHA/Np8% (Figure 5A,C). The surface of the DPBHA/Np5% (Figure 5B) was characterized by a greater disorganization of the grains, thus presenting a fractured surface pattern that is evidently different from

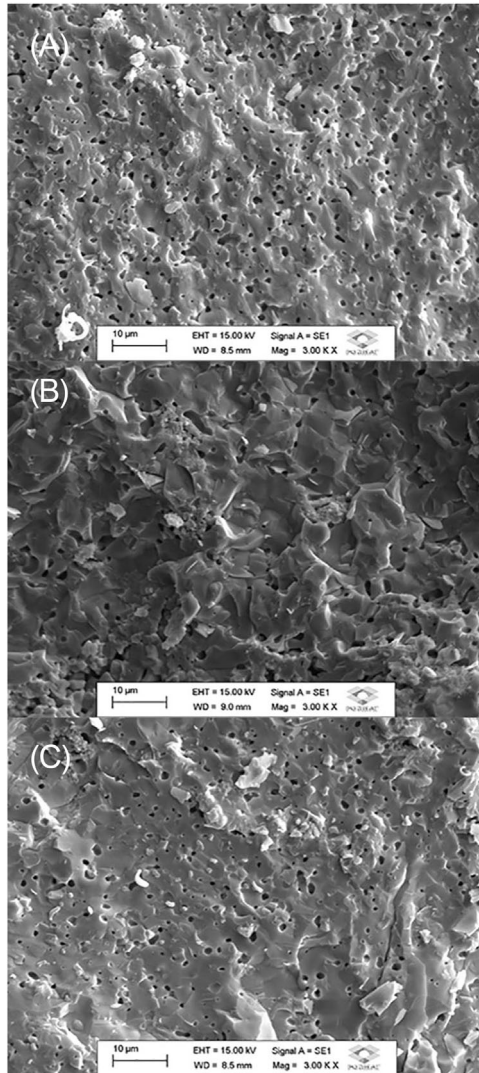


FIGURE 5 Field emission scanning electron microscope (FE-SEM) of (A) dense polycrystalline bovine hydroxyapatite (DPBHA), (B) DPBHA/Np5%, and (C) DPBHA/Np8%

that of the others. We can also notice an apparently greater cohesion among the grains of the specimens of the pure ceramic and DPBHA/Np8% groups.

EDS analyses were presented in Figure 6A–C. The results of the defined localization indicated the composition of the material. The chemical elements calcium, phosphorus, oxygen, and magnesium were noticed in all the groups. Moreover, Ti was identified in the reinforced TiO₂ nanoparticle groups. The presence of gold was observed because of its use in the methodology.

For the defined location, the EDS mappings (Figures 7 and 8) show an irregularity in the distribution of Ti in the specimens of both DPBHA/Np5% and DPBHA/Np8% groups.

3.2.2 | Relative density and apparent porosity

The relative density values are summarized in Table 2. The results indicate a statistically significant difference among groups. DPBHA/Np8% group (2.9 ± 0.09 g/cm³) showed greater density than pure HA (2.7 ± 0.03 g/cm³) ($p = 0.011$) and DPBHA/Np5% (2.7 ± 0.05 g/cm³) ($p = 0.041$) groups. Pure DPBHA and DPBHA/Np5% groups showed statistical similarity in their results ($p = 0.735$).

The apparent porosity values (percentage) are summarized in Table 3. DPBHA group (0.9%) had the lowest porosity result followed by DPBHA/Np8% group (3.4%). DPBHA/Np5% group (4.5%) exhibited the highest proportion of pores.

3.2.3 | Flexural Strength (FS)

The FS data obtained from the three-point surface flexion are summarized in Table 4. The results indicate a statistically significant difference among groups. The pure DPBHA (51.7 ± 10.3 MPa) and DPBHA/Np8% (47.4 ± 6.4 MPa) groups demonstrated superior FSs, which are statistically similar to each other ($p = 0.331$). Furthermore, these two groups had significantly greater FSs than DPBHA/Np5% group (28.8 ± 3.1 MPa) ($p < 0.001$; $p < 0.001$).

3.2.4 | Fracture toughness by flexural surface fracture (FT)

The fracture toughness (K_{Ic}) and critic defect (c) data obtained are presented in Table 5. The results indicate a statistically significant difference among groups. Pure DPBHA (0.43 ± 0.01 MPa m^{1/2}) and DPBHA/Np8% (0.40 ± 0.06 MPa m^{1/2}) groups had similar greater K_{Ic} values ($p = 0.849$) but statistically different from that of DPBHA/Np5% group (0.23 ± 0.02 MPa m^{1/2}) ($p < 0.003$; $p < 0.007$, respectively).

4 | DISCUSSION

This study hypothesis was confirmed since 5% and 8% TiO₂ nanoparticles addition changed novel DPBHA microstructure, relative porosity, flexural strenght, and fracture toughness.

Previous studies with HA found both mechanical⁶ improvement when TiO₂ nanoparticle was added and biological⁵ properties comparing with pure TiO₂ and Y-TZP. Promising results on osteoblast differentiation/

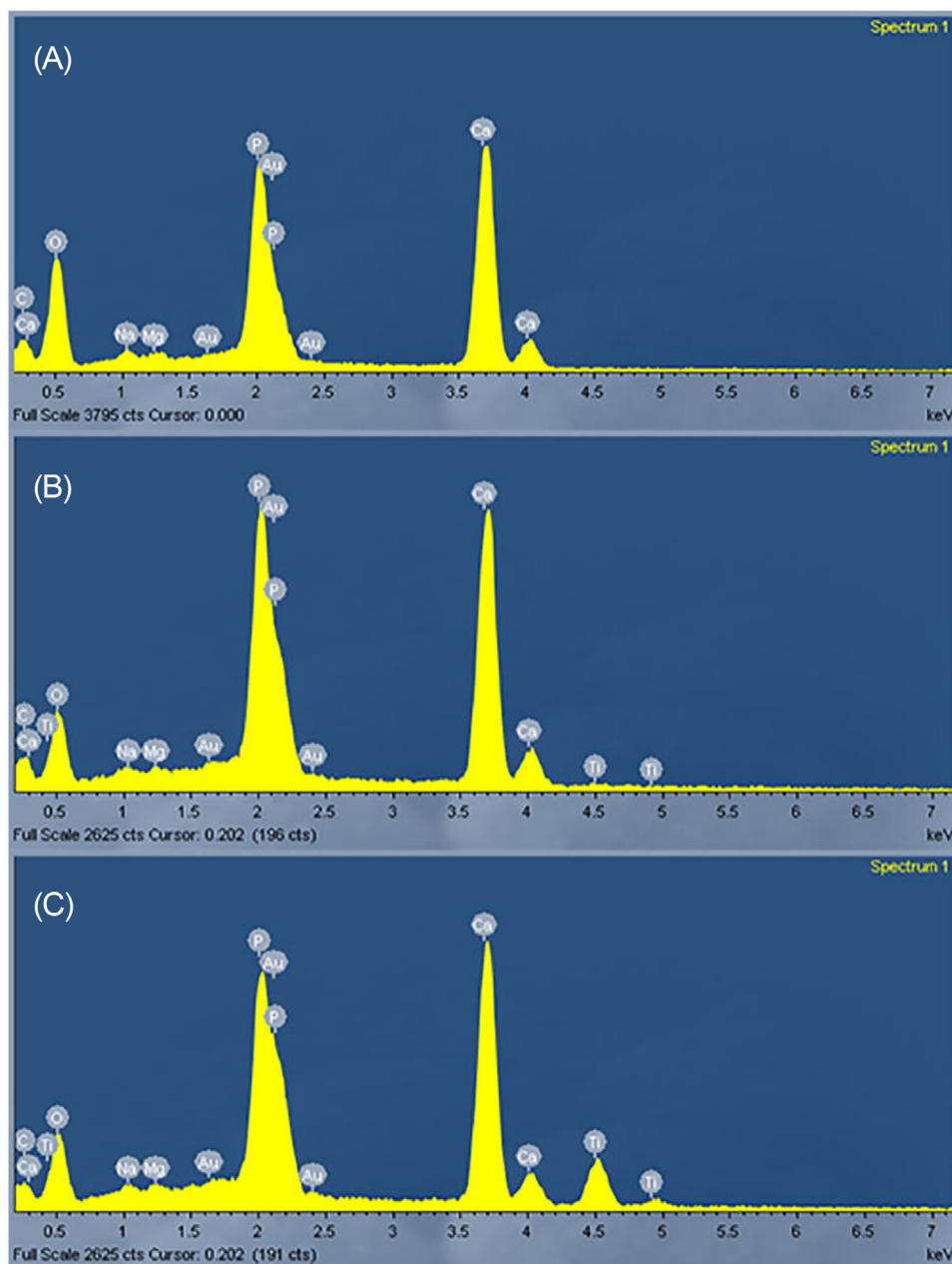


FIGURE 6 Energy dispersive spectroscopy (EDS) analysis of specimens' external surface. (A) Dense polycrystalline bovine hydroxyapatite (DPBHA), (B) DPBHA/Np5%, and (C) DPBHA/Np8%. Note the predominance of P, Ca, followed by O, Mg, and Na. The presence of C and Ti is also evidenced in TiO_2 added materials

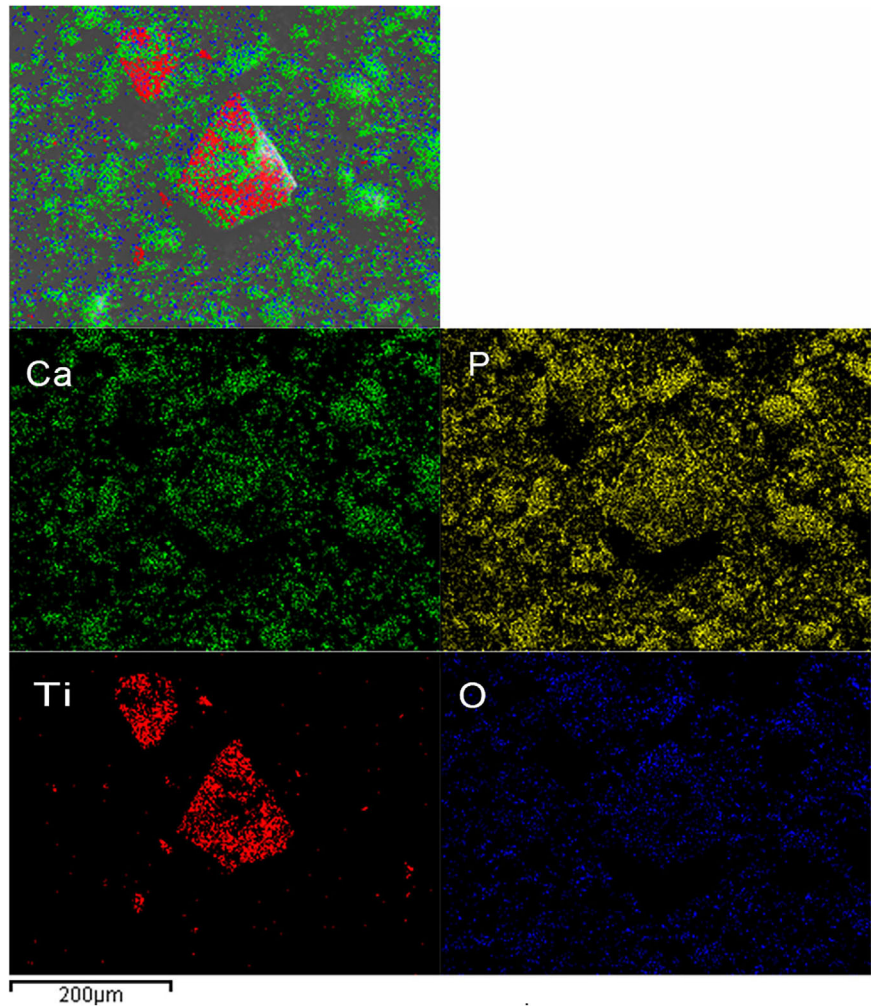
proliferation by adding TiO_2 nanoparticles into Y-TZP matrix were also achieved.¹⁶ Thus, a higher amount of TiO_2 nanoparticles was added (8%).

When mixed to a material the nanoparticles can be distributed into four modes: (1) along the grain boundaries of the matrix, (2) inside the grains of the matrix, (3) both along the grain boundaries and inside the grains, or (4) uniform distribution of both the matrix and reinforcement grains.⁴⁴ Differently from concentrated in the grains' inner or boundaries, TiO_2 nanoparticles uniformly distributed in the material matrix can increase the materials' mechanical

properties.⁴⁵ XRD characterization results showed crystallinity maintenance of HA, and FTIR characterization showed characteristic bonds, respectively, in groups added with 5% and 8% TiO_2 nanoparticles. At temperature of 1300°C, the mix of HA and TiO_2 nanoparticles did not form any secondary phases (Figures 2, 3, and 4).

The following factors influence on nanoparticle behavior as reinforcement; (1) nanoparticles' distribution; (2) nanoparticles' action on the sintering process, and (3) nanoparticles' location. In this study, EDS analysis showed that TiO_2 nanoparticle distribution was different

FIGURE 7 Energy dispersive spectroscopy (EDS) mapping of dense polycrystalline bovine hydroxyapatite (DPBHA)/Np5% group. Note that Ti was red-identified in a nonhomogeneous spreading, caused by nanoparticles' agglomeration, different from the Ca, P, and O spreading patterns



between the concentrations. DPBHA/Np5% showed lower Np homogeneity distribution than DPBHA/Np8% (Figures 7 and 8), and this could have caused the lowest FS and fracture toughness compared to the DPBHA and DPBHA/Np8%, (Tables 4 and 5).

The homogeneous distribution of the microstructures can also influence on the sintering process.⁴⁶ Generally, many materials synthesis methodologies use nanopowders processing routes. Due to their high surface area, a high predisposition to agglomeration occurs.⁴⁷ The processing of agglomerated nanopowders is commonly difficult because of the fast densification of agglomerates and slow closure of large interagglomerated pores. This fact makes difficult to eliminate interagglomerated porosity during sintering or pressing. Often the interagglomerated boundaries present higher predisposition to diffusion compared to the diffusion in the regular boundaries of the smaller grains. During the sintering process, this cluster of pores can sinter faster with a rapid growth of grains, while the nonclustered matrix has a lower sintering predisposition.^{47–49} This possible imbalance on the sintering process can impair unique properties of nanostruc-

tured materials. Moreover, adjusting the sintering time and temperature for the material can also decrease the number of pores,^{7,50} grain growth, and material densification.⁴⁶ Optimization of the temperature leads to an increase in the cohesive strength among the grains of the material, which may increase its mechanical strength.^{7,51,52}

Fractography is a crucial tool for polycrystalline ceramic inspection at fracture sites.³⁷ The marks lead to fracture origin, and their size, geometry, and characteristic areas indicate the possible critical defects that initiate fracture.⁵³ Figure 1 illustrates fractographic analyses performed to determine the critical defect. The first marks easily identified were hackle lines, which indicate the direction of crack propagation. The following could be observed: (1) arrest lines defined by the crack front shape of an arrested or momentarily hesitated crack; and, right above, (2) the mirror region, which is likely the fracture origin. Moreover, twist hackle lines generated by the primary crack were identified as well, deviating as they went around the corners with geometric irregularities.⁵⁴ Then, the critical defect could be measured to calculate fracture toughness (Table 5) of the groups using FS tests (Table 4).^{15,53,55}

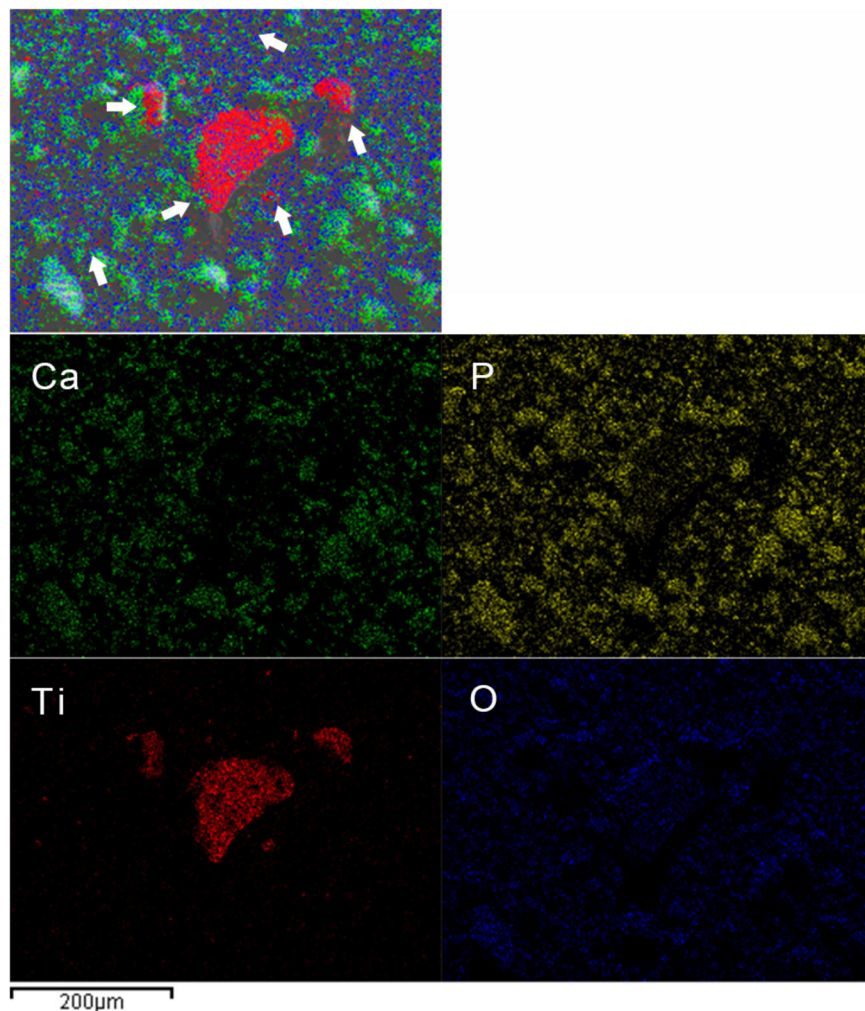


FIGURE 8 Energy dispersive spectroscopy (EDS) mapping of dense polycrystalline bovine hydroxyapatite (DPBHA)/Np8% group. Note that Ti was red-identified in a more homogeneous spreading, with less nanoparticles' agglomeration compared to the hydroxyapatite (HA)5%npTiO₂ group (white arrows)

TABLE 2 Relative density data of experimental dense polycrystalline bovine hydroxyapatite (DPBHA) ceramics by Archimedes' principle (g/cm³)

Groups	Mean (SD)
DPBHA	2.7 (0.03) b
DPBHA/Np5%	2.7 (0.05) b
DPBHA/Np8%	2.9 (0.09) a

Note: Different letters indicate statistically significant difference of 5% ($p < 0.05$).

TABLE 3 Apparent porosity data of experimental dense polycrystalline bovine hydroxyapatite (DPBHA) ceramics by Archimedes' principle (%)

Groups	%
DPBHA	0.9
DPBHA/Np5%	4.5
DPBHA/Np8%	3.4

This study showed similar critical defect means of 44.4, 44.0, and 40.0 µm for pure BPBHA, DPBHA/Np5%, and

TABLE 4 Flexural strength data of experimental dense polycrystalline bovine hydroxyapatite (DPBHA) (MPa)

Groups	Mean (SD)
DPBHA	51.7 (10.3) a
DPBHA/Np5%	28.8 (3.1) b
DPBHA/Np8%	47.4 (6.4) a

Note: Different letters indicate statistically significant difference of 5% ($p < 0.05$).

TABLE 5 Critical defect (c) and fracture toughness (K_{Ic}) data of experimental dense polycrystalline bovine hydroxyapatite (DPBHA)

	DPBHA	DPBHA/Np5%	DPBHA/Np8%
c (µm)	44.4	44.0	40.0
K _{Ic} (MPa m ^{1/2})	0.43 (0.01) a	0.23 (0.02) b	0.40 (0.06) a

Note: Different letters indicate statistically significant difference of 5% ($p < 0.05$).

DPBHA/Np8%, respectively. It is important to note that according to the Griffith–Irwin theory,^{39,40} the greater the FS and the lower critical defect size, the greater would be

the fracture toughness. Therefore, it was assumed that a crack deflection mechanism could increase the material fracture toughness of modified HA.¹⁹

DPBHA/Np8% showed higher apparent density than DPBHA and DPBHA Np5% (Table 2), which was in accordance with its apparent porosity (3.4%), revealed by SEM images (Figure 4). Nanoparticles addition increased microstructure density by controlling the grain growth of the material and resulting in smaller grains.^{22,23}

The grain sizes increased with gas diffusion within the pores during the sintering process. Pores have direct relation with the structure, grain growth, and higher ceramic grain size.^{46,51,52} The higher number of particles, the higher is the number of pores.^{7,50} Although excessive porosity can impair the mechanical characteristics of materials, some degree of porosity can positively influence the characteristics of a biomaterial, especially when a biomaterial is designed for use in implantology.⁵⁶

5 | CONCLUSIONS

Within the scope of this in vitro study, the following conclusions can be drawn:

With the physical modification obtained by 8% TiO₂ nanoparticle addition in HA matrix, this composite is considered as the most promising material match of the present study. The TiO₂ addition in 8% can be considered as reinforcement particle since it did not jeopardize FS of pure HA and increased the relative density, despite its apparent porosity. Furthermore, TiO₂ seems to be a potential nanostructure on achievement of osteoblast proliferation. This feature highlights the choice of material for mixing in HA matrix for use in dental implants. Matching both the properties of HA with those of TiO₂, and the microstructural findings through the ceramic composite obtained, it is proposed to carry out an adaptation in the processing parameters and proceed with the synthesis of this promising sustainable material.

ACKNOWLEDGMENT


The authors are grateful for the financial support provided by the São Paulo Research Foundation (FAPESP; process numbers: 2020/01715-7, 2018/23639-0 and 2013/07296-2; CDMF/CEPID/FAPESP) and the National Council for Scientific and Technological Development (CNPq; process number: 154705/2015-2).

ORCID

Lucas José de Azevedo-Silva  <https://orcid.org/0000-0002-6636-8022>

Brunna Mota Ferrairo  <https://orcid.org/0000-0002-8121-3002>

David Santos Souza Padovini  <https://orcid.org/0000-0003-4231-8802>

Leonardo Francisco Gonçalves Dias  <https://orcid.org/0000-0002-1921-1727>

Rogério Erbereli  <https://orcid.org/0000-0003-0753-8172>

Carlos Alberto Fortulan  <https://orcid.org/0000-0002-2259-9910>

Paulo Noronha Lisboa-Filho  <https://orcid.org/0000-0002-7734-4069>

José Henrique Rubo  <https://orcid.org/0000-0003-1595-845X>

Ana Flávia Sanches Borges  <https://orcid.org/0000-0002-0349-2050>

REFERENCES

- Eanes ED. Crystal-growth of mineral phases in skeletal tissues. *Prog Cryst Growth Ch.* 1980;3(1):3–15.
- Oguchi H, Ishikawa K, Mizoue K, Seto K, Eguchi G. Long-term histological-evaluation of hydroxyapatite ceramics in humans. *Biomaterials* 1995;16(1):33–8.
- Szabo-Júnior AM. Environmental education and waste management. 3rd ed. São Paulo: Rideel; 2010.
- Jabbour ABL, Jabbour CJC. Environmental management in organizations: fundamentals and trends. São Paulo: Atlas; 2013.
- Pires LA, Fortulan CA, Rontani RM. Wettability and pre-osteoblastic behavior evaluations of a dense bovine hydroxyapatite ceramic. *J Oral Sci.* 2020;62(3):259–64.
- Pires LA, Silva LJA, Ferrairo BM, Erbereli R, Lovo JFP, Ponce Gomes O, et al. Effects of ZnO/TiO₂ nanoparticle and TiO₂ nanotube additions to dense polycrystalline hydroxyapatite bioceramic from bovine bones. *Dent Mater.* 2020;36(2):e38–46.
- Miranda RBP, Miranda WG, Lazar DRR, Ussui V, Marchi J, Cesar PF. Effect of titania content and biomimetic coating on the mechanical properties of the Y-TZP/TiO₂ composite. *Dent Mater.* 2018;34(2):238–45.
- Yilmaz H, Aydin C, Gul BE. Flexural strength and fracture toughness of dental core ceramics. *J Prosthet Dent.* 2007;98:120–8.
- Marrelli M, Maletta C, Inchingolo F, Alfano M, Tatullo M. Three-point bending tests of zirconia core/veneer ceramics for dental restorations. *Int J Dent.* 2013;2013:1–5.
- Guazzato M, Albakry M, Ringer SP, Swain MV. Strength, fracture toughness and microstructure of a selection of all-ceramic materials. Part II. Zirconia-based dental ceramics. *Dent Mater.* 2004;20:449–56.
- Wang RR, Lu CL, Wang G, Zhang DS. Influence of cyclic loading on the fracture toughness and load bearing capacities of all-ceramic crowns. *Int J Oral Sci.* 2014;6:99–104.
- Jodha KS, Salazar Marrocho SM, Scherrer SS, Griggs JA. Fractal analysis at varying locations of clinically failed zirconia dental implants. *Dent Mater.* 2020;36(8):1052–8.
- Scherrer SS, Mekki M, Crottaz C, Gahlert M, Romelli E, Marger L, et al. Translational research on clinically failed zirconia implants. *Dent Mater.* 2019;35(2):368–88.
- Passos SP, Nychka JA, Major P, Linke B, Flores-Mir C. In vitro fracture toughness of commercial Y-TZP ceramics: a systematic review. *J Prosthodont.* 2015;24(1):1–11.

15. Cesar PF, Della Bona A, Scherrer SS, Tholey M, van Noort R, Vichi A, et al. ADM guidance-ceramics: fracture toughness testing and method selection. *Dent Mater.* 2017;33(6):575–84.
16. de Paula Miranda RB, Leite TP, Pedroni ACF, Marques MM, de Lima NB, Marchi J, et al. Effect of titania addition and sintering temperature on the microstructure, optical, mechanical and biological properties of the Y-TZP/TiO₂ composite. *Dent Mater.* 2020;36(11):1418–29.
17. Lopes ACO, Coelho PG, Witek L, Benalcázar Jalkh EB, Gênova LA, Monteiro KN, et al. Microstructural, mechanical, and optical characterization of an experimental aging-resistant zirconia-toughened alumina (ZTA) composite. *Dent Mater.* 2020;36(12):e365–74.
18. Sun Z, Zhao J, Wang X, Cui E, Yu H. Reinforcing mechanisms of graphene and nano-TiC in Al₂O₃-based ceramic-tool materials. *Nanomaterials (Basel).* 2020;10(9):1815.
19. Faber KT, Evans AG. Crack deflection processes-I. Theory *Acta Metall.* 1983;31(4):565–76.
20. Fortulan CA. Alumina-zirconia composite: obtaining through colloidal conformation and microstructural characterization. São Carlos: Federal University of São Carlos; 1999.
21. Fang Z, Feng QL, Tan RW. In-situ grown hydroxyapatite whiskers reinforced porous HA bioceramic. *Ceram Int.* 2013;39(8):8847–52.
22. Ravarian R, Moztarzadeh F, Hashjin MS, Rabiee SM, Khoshakhlagh P, Tahriri M. Synthesis, characterization and bioactivity investigation of bioglass/hydroxyapatite composite. *Ceram Int.* 2010;36(1):291–7.
23. Yelten A, Yilmaz S, Oktar FN. Sol-gel derived alumina-hydroxyapatite-tricalcium phosphate porous composite powders. *Ceram Int.* 2012;38(4):2659–65.
24. Ramires PA, Romito A, Cosentino F, Milella E. The influence of titania/hydroxyapatite composite coatings on in vitro osteoblasts behaviour. *Biomaterials* 2001;22(12):1467–74.
25. Silva VV, Lameiras FS, Domingues RZ. Microstructural and mechanical study of zirconia-hydroxyapatite (ZH) composite ceramics for biomedical applications. *Compos Sci Technol.* 2001;61(2):301–10.
26. Kalita SJ, Rokusek D, Bose S, Hosick HL, Bandyopadhyay A. Effects of MgO-CaO-P₂O₅-Na₂O-based additives on mechanical and biological properties of hydroxyapatite. *J Biomed Mater Res A.* 2004;71(1):35–44.
27. Ning CQ, Zhou Y. On the microstructure of biocomposites sintered from Ti, HA and bioactive glass. *Biomaterials* 2004;25(17):3379–87.
28. Nath S, Dey A, Mukhopadhyay AK, Basu B. Nanoindentation response of novel hydroxyapatite-mullite composites. *Mat Sci Eng A.* 2009;513–14:197–201.
29. Rahman MM, Krishna KM, Soga T, Jimbo T, Umeno M. Optical properties and X-ray photoelectron spectroscopic study of pure and Pb-doped TiO₂ thin films. *J Phys Chem Sol.* 1999;60(2):201–10.
30. Zhao Y, Li C, Liu X, Gu F, Jiang H, Shao W, et al. Synthesis and optical properties of TiO₂ nanoparticles. *Mater Let.* 2007;61(1):79–83.
31. Diebold U. The surface science of titanium dioxide. *Surf Sci Rep.* 2003;48(5–8):53–229.
32. Gupta SM, Tripathi M. Review of TiO₂ nanoparticles. *Chin Sci Bull Kexue Tongbao.* 2011;56(16):1639–57.
33. Kuo HN, Chou JH, Liu TK. Microstructure and mechanical properties of microwave sintered ZrO₂ bioceramics with TiO₂ addition. *Appl Bionics Biomech.* 2016;2016:2458685.
34. Weng MH, Lin CX, Huang CS, Tsai CY, Yang RY. Improved microstructure and hardness properties of low-temperature microwave-sintered Y₂O₃ stabilized ZrO₂ ceramics with additions of nano TiO₂ powders. *Materials* 2020;13(7):1546.
35. Arruda LB, Santos CM, Orlandi MO, Schreiner WH, Lisboa PN. Formation and evolution of TiO₂ nanotubes in alkaline synthesis. *Ceram Int.* 2015;41(2):2884–91.
36. International Standard ISO 6872, Dentistry – ceramic materials. Geneva, Switzerland: International Standards Organization; 2015.
37. Ramos CM, Cesar PF, Bonfante EA, Rubo JH, Wang L, Borges AF. Fractographic principles applied to Y-TZP mechanical behavior analysis. *J Mech Behav Biomed Mater.* 2016;57:215–23.
38. ASTM. Standard practice for fractography and characterization of fracture origins in advanced ceramics. West Conshohocken, PA: ASTM; 2003.
39. Griffith AA. The phenomena of rupture and flow in solids. *Philos Trans R Soc.* 1992;221:35.
40. Irwin GR. Analysis of stresses and strains near the end of a crack transversing a plate. *J Appl Mech.* 1957;24:361–64.
41. Veiga A, Castro F, Reis C, Sousa A, Oliveira AL, Rocha F. Hydroxyapatite/sericin composites: a simple synthesis route under near-physiological conditions of temperature and pH and preliminary study of the effect of sericin on the biomineralization process. *Mater Sci Eng C.* 2020;108:110400.
42. Pekounov Y, Chakarova K, Hadjiivanov K. Surface acidity of calcium phosphate and calcium hydroxyapatite: FTIR spectroscopic study of low-temperature CO adsorption. *Mater Sci Eng C.* 2009;29(4):1178–81.
43. Huo X, Liu P, Zhu J, Liu X, Ju H. Electrochemical immunosensor constructed using TiO₂ nanotubes as immobilization scaffold and tracing tag. *Biosens Bioelectron.* 2016;85:698–706.
44. Saheb N, Qadir NU, Siddiqui MU, Arif AFM, Akhtar SS, Al-Aqeeli N. Characterization of nanoreinforcement dispersion in inorganic nanocomposites: a review. *Materials* 2014;7(6):4148–81.
45. Yamamoto G, Hashida T. Carbon nanotube reinforced alumina composite materials. In: Hu N, editor. *Composites and their properties.* Rijeka, Croatia: InTech; 2012.
46. Ju H, Ning K, Lu K. Sintering behaviors of micron-sized ceramic rod features. *Acta Mater.* 2018;144:534–42.
47. Maximenko AL, Olevsky EA, Grigoryev EG. Homogenization of biporous agglomerated powder structures during high-temperature consolidation. *J Am Ceram Soc.* 2015;98(11):e3445–52.
48. Maximenko AL, Olevsky EA, Shtern MB. Plastic behavior of agglomerated powder. *Comp Mater Sci.* 2008;43(4):e704–9.
49. Li W, Olevsky EA, Khasanov OL, Back CA, Izhevyanov O, Opperman J, et al. Spark plasma sintering of agglomerated vanadium carbide powder. *Ceram Int.* 2015;41(3):e3748–59.
50. Miao X, Sun D, Hoo PW, Liu J, Hu Y, Chen Y. Effect of titania addition on yttria-stabilized tetragonal zirconia ceramics sintered at high temperatures. *Ceram Int.* 2004;30(6):1041–7.
51. Eichler J, Rödel J, Eisele U, Hoffman M. Effect of grain size on mechanical properties of submicrometer 3Y-TZP: fracture

- strength and hydrothermal degradation. *J Am Ceram Soc.* 2007;90(9):2830–6.
52. Stawarczyk B, Özcan M, Hallmann L, Ender A, Mehl A, Hammerlet C. The effect of zirconia sintering temperature on flexural strength, grain size and contrast ratio. *Clin Oral Investig.* 2013;17(1):269–74.
53. Rice RW. Fractographic determination of K_{Ic} and effects of microstructural stresses in ceramics. *Fractography of glasses and ceramics, ceramic transactions.* Am Ceram Soc. 1991;38:17.
54. Quinn GD. NIST Recommended Practice Guide: Fractography of Ceramics and Glasses, 2nd edition, Special Publication (NIST SP), National Institute of Standards and Technology, Gaithersburg, MD, 2016.
55. Fujishima A, Zhang XT. Titanium dioxide photocatalysis: present situation and future approaches. *C R Chim.* 2006;9(5–6):750–60.
56. Jakus AE, Geisendorfer NR, Lewis PL, Shah RN. 3D-printing porosity: a new approach to creating elevated porosity materials and structures. *Acta Biomater.* 2018;72:94–109.

How to cite this article: de Azevedo-Silva LJ, Ferrairo BM, Pires LA, Padovini DSS, Dias LFG, Erbereli R, et al. Novel 8%-TiO₂-nanoparticle-reinforced dense polycrystalline bovine hydroxyapatite bioceramic. *Int J Ceramic Eng Sci.* 2022;4:158–169.

<https://doi.org/10.1002/ces2.10127>